COMMUNICATIONS PHYSICS

ARTICLE

https://doi.org/10.1038/s42005-019-0120-1 OPEN

Negative capacitance from the inductance of ferroelectric switching

Po-Hsien Cheng[1], Yu-Tung Yin[1], I-Na Tsai[1], Chen-Hsuan Lu[1], Lain-Jong Li[2], Samuel C. Pan[3], Jay Shieh[1], Makoto Shiojiri[4] & Miin-Jang Chen[1,5]

Negative capacitance (NC) has been proposed to realize sub-Boltzmann steep-slope transistors in recent years. We provide experimental evidences and theoretical view for ferroelectric NC and inductance induced by polarization switching, based on an as-deposited nanoscale ferroelectric zirconium oxide (ZrO_2) layer (nano-*f*-ZrO_2). The experimental results are demonstrated in nano-*f*-ZrO_2, including resistor–inductor–capacitor oscillations, positive reactance in Nyquist impedance plot, enhancement of capacitance, and sub-60 mV/dec subthreshold swing of nanoscale transistors. The theoretical analysis shows that ferroelectric polarization switching yields an effective electromotive force which is similar in behavior to Lenz's law, leading to inductive and NC responses. Nano-beam electron diffraction reveals ferroelectric multi-domains in nano-*f*-ZrO_2. Under small-signal operation, the switching of net polarization variation in ferroelectric multi-domains contributes to the ferroelectric inductance and NC. Nano-*f*-ZrO_2 provides a pronounced inductance compared to conventional inductors, which would have impacts in a variety of applications including transistors, filters, oscillators, and radio-frequency-integrated circuits.

[1] Department of Materials Science and Engineering, National Taiwan University, Taipei, Taiwan, ROC. [2] Taiwan Semiconductor Manufacturing Company, Hsinchu, Taiwan, ROC. [3] TSMC-NTU Research Center, National Taiwan University, Taipei, Taiwan, ROC. [4] Kyoto Institute of Technology, Kyoto, Japan. [5] Graduate Institute of Electronics Engineering, National Taiwan University, Taipei, Taiwan, ROC. Correspondence and requests for materials should be addressed to M.-J.C. (email: mjchen@ntu.edu.tw)

Ferroelectric negative capacitance (NC) has been proposed as a promising method to overcome the Boltzmann limit for next-generation energy-efficient transistors[1,2]. Steep-slope transistors, with subthreshold swing (SS) below 60 mV/dec due to the NC effect during ferroelectric polarization switching, have been experimentally demonstrated in recent years[3–17]. From the viewpoint of the phase of impedance, the behavior of NC seems to be “inductance-like”[3]. Among these studies, however, experimental evidences of the inductance originating from ferroelectric polarization switching have not been clearly demonstrated.

The ferroelectric NC has been mainly demonstrated with HZO ($Hf_{0.5}Zr_{0.5}O_2$) in previous reports[9,18–20], where various crystalline phases exist in HZO. Thus, the post-deposition annealing (PDA) at high temperatures of 500–1000 °C is normally required to enrich the ferroelectric orthorhombic phase in HZO[21–23]. Furthermore, the PDA temperature down to 450 °C has been realized to achieve ferroelectricity in Gd-doped hafnium oxide (HfO_2)[23]. The high-temperature PDA, however, is generally detrimental to the semiconductor process integration. Therefore, it is highly favorable to produce ferroelectric thin films without PDA treatments. In fact, the highly crystalline zirconium oxide (ZrO_2) with strong ferroelectric responses has been successfully achieved without the need to perform PDA treatments in our previous study[24].

In this paper, we report experimental observations of the inductance caused by ferroelectric polarization switching under both large- and small-signal operations. Large-signal resistor–inductor–capacitor (RLC) oscillations in time domain and a positive imaginary impedance in the Nyquist plot of metal–ferroelectric–metal (MFM) structures are observed, indicating the presence of significant inductance in the nanoscale ferroelectric ZrO_2 layer (abbreviated as nano-f-ZrO_2). We theoretically show that ferroelectric polarization switching produces an “effective ferroelectric-induced electromotive force (emf),” which results in a decrease of the voltage drop across the ferroelectric layer. This effective ferroelectric-induced emf behaves like the emf predicted by Lenz’s law, which is opposite to the applied voltage, and so contributes to the inductance and NC effect. The NC induced by ferroelectric polarization switching is also manifested by the enhancement of small-signal capacitance of a paraelectric capacitor as connected in series with a ferroelectric capacitor. The ferroelectric multi-domains in a nanoscale ZrO_2 layer, which are responsible for the small-signal operation of the ferroelectric inductance and NC, are observed via the nano-beam electron diffraction (NBED) characterization. The NC junctionless transistor (NC-JLT) with SS <60 mV/dec operated under a large drain voltage, along with the hysteresis-free operation, is also demonstrated.

Results

As-deposited f-ZrO_2 with NC. The as-deposited ZrO_2 was used as the nanoscale ferroelectric layer in this study. Supplementary Figure 1 (Supplementary Information, Note 1) shows the polarization–electric field (P–E) hysteresis loop of the Pt/ZrO_2(12 nm)/Pt MFM structure, proving the existence of ferroelectricity of the as-deposited nanoscale ZrO_2 layer. The as-deposited nano-f-ZrO_2 was integrated into the gate stack in the nanoscale Si JLT as schematically shown in Fig. 1a. The top view of the Si channel (~70 nm in length) and contact pads taken by helium ion microscopy is shown in Supplementary Figure 2 (Supplementary Information, Note 1). Figure 1b, c shows the cross-sectional transmission electron microscope (TEM) and scanning electron microscope (SEM) images of the channel and the gate stack, revealing the Si channel with an Ω-shaped gate on a silicon-on-insulator substrate. The gate structure comprises a HfO_2(~6 nm) high-K dielectric layer stacked with an as-deposited TiN(~15 nm)/Pt(~70 nm)/f-ZrO_2(~12 nm)/TiN(~15 nm)/Pt (~70 nm) MFM structure, as shown schematically in Fig. 1a. Figure 1d shows the pronounced ferroelectric characteristics of a separately prepared MFM test structure with the same MFM stacking as shown in Fig. 1a. Note that the TiN layer is adopted here to increase the adhesion of the overlaying Pt layer for improving the yield of fabricated transistors. Figure 1e shows the forward and backward I_d (drain current)–V_{gs} (gate voltage) curves of the NC-JLT. The I_d–V_{ds} (drain voltage) is provided in Supplementary Figure 3 (Supplementary Information, Note 3). The hysteresis-free I_d–V_{gs} characteristics are observed, which can be deduced from the positive overall capacitance as required by the stability of NC[4,6,8–11,13,14,16]. The plot of SS at $V_{ds} = 1$ V versus V_{gs} is shown in Fig. 1f, indicating SS <60 mV/dec and a minimum SS of 46 mV/dec. (The I_d–V_{gs} curve of the JLT without the f-ZrO_2 layer is shown in Supplementary Information, Note 4 for a comparison.) This result demonstrates the sub-60 mV/dec SS in NC transistors operated at a high V_{ds} (1 V), and reveals the NC effect of nano-f-ZrO_2 under the large-signal on-off operation of transistors.

Ferroelectric inductance with large-signal switching operation. Figure 2a, b shows the transient responses of the as-deposited Pt/ZrO_2(12 nm)/Pt MFM structure, that is, the time–domain voltage and current waveforms (V_{FE} and I_{FE}) across nano-f-ZrO_2 under the excitation of a voltage pulse $V_{in} = 0.5$ and 2 V. In principle, the paraelectric insulator in metal–insulator–metal structures exhibits typical resistor–capacitor (RC) charging and discharging features. However, the non-RC responses, that is, the significant damped oscillations of V_{FE} and I_{FE} are clearly observed in Fig. 2a, b. The overshoot/undershoot of V_{FE} and the damped oscillation of I_{FE} agree well with typical characteristics of the underdamped RLC response[25]. As compared with Fig. 2a ($V_{in} = 0.5$V), the suppressed oscillations of V_{FE} and I_{FE} in Fig. 2b ($V_{in} = 2$ V) are ascribed to a decrease of the parallel resistance across nano-f-ZrO_2 due to an increase of the leakage at a higher V_{in}. Therefore, Fig. 2a, b indicate the existence of the inductive component in nano-f-ZrO_2. In order to confirm the existence of inductance, an impedance analyzer was used to probe the ZrO_2 MFM structure. Figure 2c shows the Nyquist plot of the complex impedance ($Z_r + jZ_i$) of the Pt/ZrO_2(12 nm)/Pt MFM structure. An inductive loop, characterized by positive imaginary impedance, appears in the Nyquist plot. Therefore, the electrical characteristics of ZrO_2 MFM structure can be described in terms of an equivalent circuit containing inductance[26–30], confirming the presence of inductance in nano-f-ZrO_2. Recently, the impedance behaviors of ferroelectric-like materials have been noticed in the metal-halide perovskite solar cells[31–33], and their Nyquist plots are similar to that shown in Fig. 2c. The analysis of impedance spectra of these perovskite solar cells has also revealed that an inductive component is present in the equivalent circuit[31].

The physical origin of ferroelectric inductance can be derived from Maxwell’s equations (Supplementary Information, Notes 6–7). The charge redistribution caused by ferroelectric polarization switching leads to a decrease of the voltage drop across the ferroelectric layer, which is terminologically denoted as the “effective ferroelectric-induced emf”. As schematically illustrated in Fig. 2d, the polarity of this effective ferroelectric-induced emf is opposite to the applied voltage, which is similar in behavior to Lenz’s law, indicating that the induced emf acts against the applied voltage. Therefore, the effective ferroelectric-induced emf gives rise to the inductive responses of the ferroelectric layer. Accordingly, a simple equivalent RLC circuit of the ferroelectric layer is proposed in Supplementary Figure 9 (Supplementary

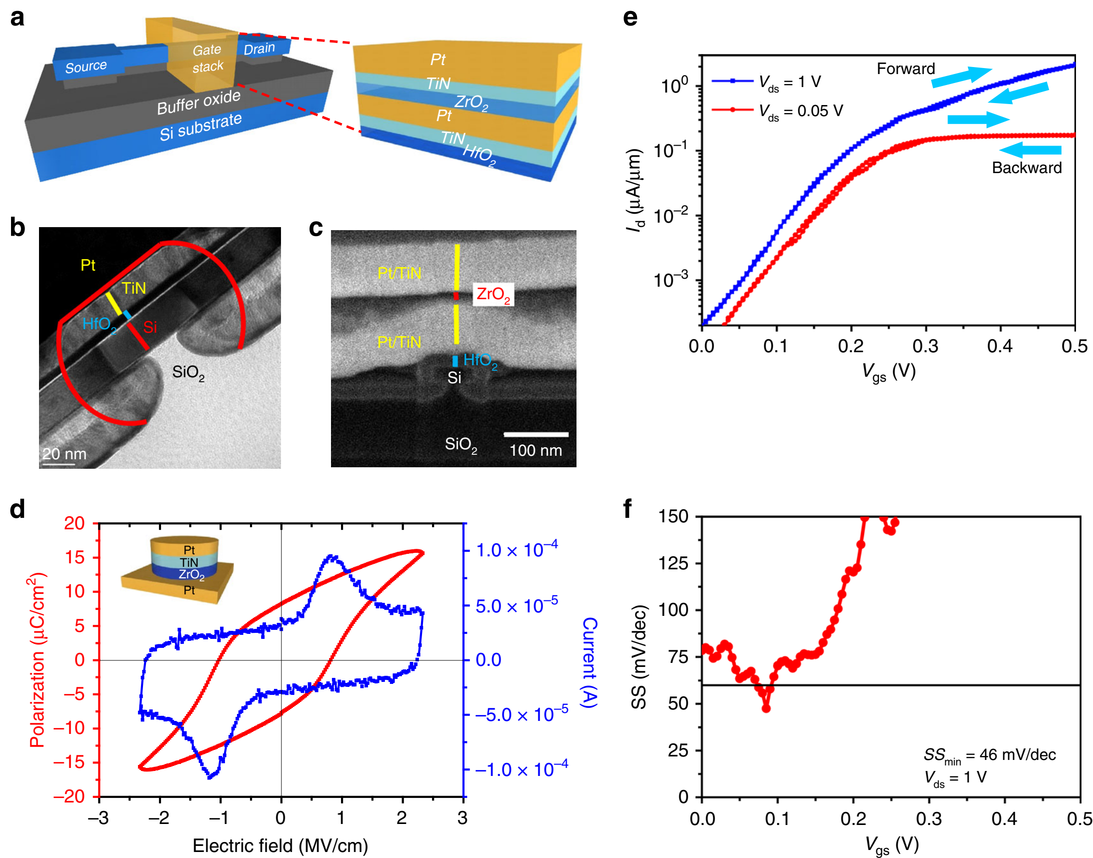

Fig. 1 Negative-capacitance Si junctionless transistor (NC-JLT) and the gate stack. **a** The schematic of the transistor and the layer structure of the gate stack. **b**, **c** are the cross-sectional transmission electron microscope (TEM) and scanning electron microscope (SEM) images of the Si channel and the gate stack. **d** Ferroelectric characteristics of the as-deposited zirconium oxide (ZrO_2) metal-ferroelectric-metal (MFM) structure, exhibiting significant polarization-electric field (*P*–*E*) hysteresis loop and switching current. The inset shows the schematic diagram of the as-deposited ZrO_2 MFM structure. **e**, **f** Electrical characteristics of the NC-JLT. **e** The forward and backward I_d–V_{gs} curves at $V_{ds} = 0.05$ and 1 V, respectively, indicating the hysteresis-free I_d–V_{gs} characteristics. **f** The subthreshold swing (SS) as a function of V_{gs} at a large drain voltage of $V_{ds} = 1$V, revealing sub-60 mV/dec SS with a minimum value of 46mV/dec

Information, Note 8), where the inductor describes the decrease in the voltage drop across the ferroelectric capacitor during ferroelectric polarization switching. Hence, the magnitude of the inductance can be estimated by curve fitting to the I_{FE} waveforms based on this equivalent circuit as shown in Supplementary Figure 11 (Supplementary Information, Note 8). The inductance density of nano-*f*-ZrO_2 is approximately on the order of 10 mH/cm². As compared with conventional inductors, which are of spiral geometries and suffer severely from large occupied areas and low inductance densities (<10 μH/cm²)[34], nano-*f*-ZrO_2 offers a much larger inductance density. Because of the presence of the inductance and capacitance in the simple equivalent circuit of the ZrO_2 MFM structure as shown in Supplementary Figure 9, nano-*f*-ZrO_2 can serve as the filters/oscillators/resonators in the applications including radio-frequency (RF) communication and signal-processing systems[25].

NC and ferroelectric inductance. The connection between NC and the effective ferroelectric-induced emf can be understood as follows:

$$i_D = C_{FE}\frac{\Delta V}{\Delta t}, \quad (1)$$

where i_D is the displacement current through the ferroelectric layer with the capacitance C_{FE}, Δt is the time scale of ferroelectric polarization switching, and ΔV is the change of the voltage drop across the ferroelectric layer caused by polarization switching. Since the effective ferroelectric-induced emf leads to a decrease of the voltage drop across the ferroelectric layer, that is, $\Delta V<0$, Eq. 1 indicates $C_{FE} < 0$.

NC observed with small-signal switching operation. The evidence of NC is also demonstrated by the enhancement of the small-signal capacitance of a paraelectric HfO_2 capacitor as connected in series with a nano-*f*-ZrO_2 capacitor. The schematic diagrams and cross-sectional TEM images of the capacitor structures under test are shown in Fig. 3a, Supplementary Figure 12, and Supplementary Figure 13 (Supplementary Information, Note 9). Figure 3b compares the *P*–*E* characteristics of the as-deposited paraelectric HfO_2, paraelectric ZrO_2 (*p*-ZrO_2), and *f*-ZrO_2 layers. Note that the paraelectric/ferroelectric properties of the as-deposited nanoscale ZrO_2 layer can be controlled by the process conditions of atomic layer deposition (ALD) as described in Materials and methods. Figure 3c shows the small-signal capacitance of the three capacitor structures, in which the dielectric layers are HfO_2, *p*-ZrO_2 in series with HfO_2 (denoted as *p*-ZrO_2/HfO_2), and *f*-ZrO_2 in series with HfO_2 (denoted as *f*-ZrO_2/HfO_2), respectively. The capacitance of the *p*-ZrO_2/HfO_2 structure is lower than that of the HfO_2 capacitor, as expected from the series connection of two paraelectric capacitors.

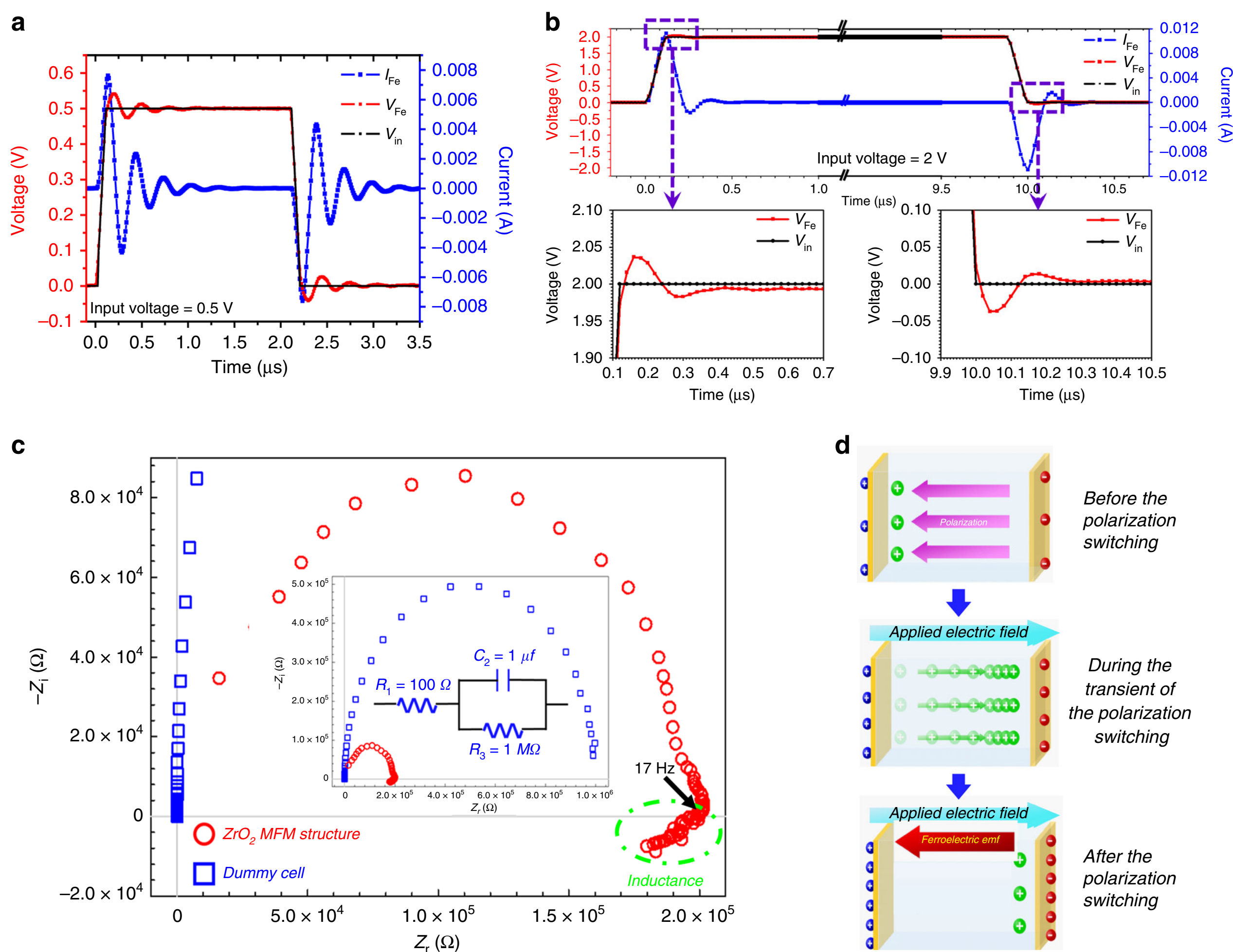

Fig. 2 Experimental observations and schematic illustration of ferroelectric inductance. **a**, **b** Transient voltage and current responses of the as-deposited zirconium oxide (ZrO_2) metal–ferroelectric–metal (MFM) structure under the excitation of a voltage pulse. The black, red, and blue lines are the waveforms of the input voltage (V_{in}), the voltage cross the MFM structure (V_{FE}), and the current through the MFM structure (I_{FE}), respectively. **a** shows V_{FE} and I_{FE} waveforms under $V_{in} = 0.5$ V. **b** shows V_{FE} and I_{FE} waveforms under $V_{in} = 2$ V, with magnification of V_{FE} at the rising and falling edge. The damped oscillation of I_{FE} and the overshoot/undershoot of V_{FE} indicate the inductive responses of the ferroelectric layer. The enlarged figure is shown in Supplementary information, Supplementary Note 5. **c** Nyquist impedance plot of the as-deposited Pt/ZrO_2(12 nm)/Pt MFM structure, where Z_r and Z_i are the real and imaginary parts of the complex impedance. The measurement was carried out by an impedance analyzer in the frequency range from 1 MHz to 10 mHz at a 1 V direct-current (DC) voltage and a 10 mV alternate current (AC) perturbation. The inset shows the Nyquist plot of the resistor–capacitor (RC) dummy cell comprising a series resistor (100 Ω) and an RC element (1 μF) capacitance and 1 MΩ resistance in parallel). The dummy cell was provided by Metrohm AUTOLAB® for standard test. It can be seen that an RC circuit gives a semi-circle of negative imaginary impedance in the Nyquist plot. As compared with the RC dummy cell, positive imaginary impedance is seen in the lower part of the Nyquist plot, indicating the presence of inductance in the equivalent circuit of nano-*f*-ZrO_2. **d** Schematic diagram of the effective ferroelectric-induced electromotive force (emf) originating from ferroelectric polarization switching. This effective ferroelectric-induced emf behaves like the emf predicted by Lenz's law, which opposes the applied electric field and so contributes to the inductance of the ferroelectric layer

However, the capacitance increases (×1.1) as the HfO_2 capacitor is connected in series with the *f*-ZrO_2 capacitor (the *f*-ZrO_2/HfO_2 structure). The capacitance of the *f*-ZrO_2 layer can be estimated from Fig. 3c to be $C_{FE} = -13.70\mu F/cm^2$, (Supplementary Information, Note 10). Hence Fig. 3c gives a clear demonstration of the NC effect as a paraelectric capacitor is connected in series with a ferroelectric capacitor[4,6,12]. Figure 3d shows the small-signal capacitance of the *f*-ZrO_2/HfO_2, HfO_2, and *p*-ZrO_2/HfO_2 capacitor structures as a function of the frequency. The frequency dispersion of the capacitance is not obvious in the *f*-ZrO_2/HfO_2 capacitor in the frequency range between 10 kHz and 1 MHz, indicating that the time scale of ferroelectric polarization switching in nano-*f*-ZrO_2 is <1μs.

Discussion

Note that the capacitance shown in Fig. 3 was obtained based on the small-signal measurement at a 1 V direct-current (DC) bias and a 30 mV alternating-current (AC) perturbation. However, for a layer of ferroelectric single domain, the small-signal modulation hardly causes ferroelectric polarization switching because the amplitude of small signals is much lower than the coercive voltage for polarization switching. The ferroelectric polarization switching under small-signal operation can be understood from ferroelectric multi-domains, as illustrated in Fig. 4a. It has been reported that 180° out-of-phase ferroelectric multi-domains are favorable for the reduction of stray fields in ferroelectric layers[35,36]. (The stability of ferroelectric multi-domains is

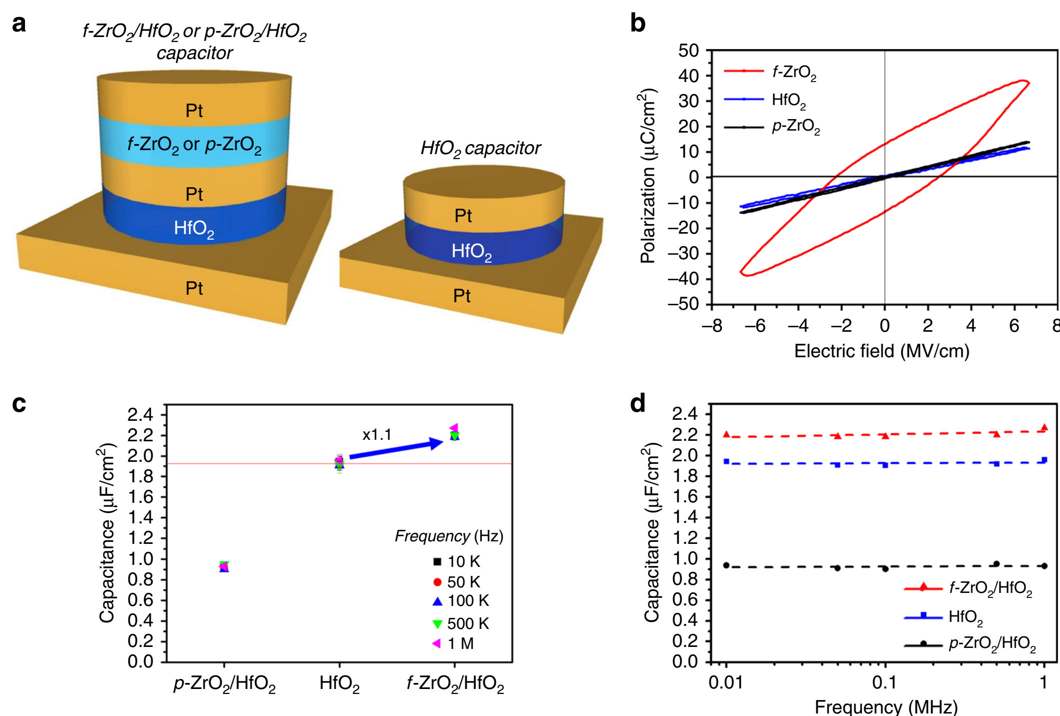

Fig. 3 Small-signal capacitance enhancement of a paraelectric hafnium oxide (HfO_2) capacitor connected in series with a zirconium oxide (ZrO_2) capacitor. **a** Schematic diagram of the ferroelectric ZrO_2 (*f*-ZrO_2)/HfO_2, *p*-ZrO_2/HfO_2, and HfO_2 capacitor structures. **b** The polarization–electric field (*P*–*E*) curves of the as-deposited paraelectric HfO_2, paraelectric ZrO_2 (*p*-ZrO_2), and *f*-ZrO_2 layers. **c** The small-signal capacitance of the *p*-ZrO_2/HfO_2, HfO_2, *f*-ZrO_2/HfO_2 capacitor structures. The capacitance was probed at a direct-current (DC) voltage of 1 V and an alternate current (AC) perturbation of 30 mV. The *f*-ZrO_2/HfO_2 capacitor exhibits capacitance enhancement (×1.1) compared with the HfO_2 capacitor, indicating the effect of negative capacitance as a paraelectric capacitor is connected in series with a ferroelectric capacitor. **d** The capacitance of the *f*-ZrO_2/HfO_2, *p*-ZrO_2/HfO_2, and HfO_2 capacitor structures as a function of the frequency from 10 kHz to 1 MHz. The capacitance is almost free of frequency dispersion

discussed in Supplementary Information, Note 11.) Hence, the polarizations in ferroelectric multi-domains are organized with alternate up and down orientations[35,36]. The DC bias generates a net polarization in ferroelectric multi-domains. The applied small-signal voltage causes elongation or compression of the polarization in each domain, resulting in the switching of the net polarization variation in the ferroelectric layer, as shown schematically in Fig. 4a.

Figure 4b shows the bright-field cross-sectional TEM image of the as-deposited Pt/ZrO_2(12 nm)/Pt MFM structure. Figure 4c shows an NBED pattern that was taken by an electron beam focused mainly into an area enclosed by the yellow box in Fig. 4b. Ferroelectricity has been considered as originating typically from the orthorhombic phase[19]. However, because of the overlap between low-symmetry nanoscale domains, an apparent "average" or "pseudo" cubic symmetry would be observed under the NBED characterization of the nanoscale ZrO_2 layer[37,38]. Since Fig. 4c is in good agreement with the simulated diffraction spots generated from the standard cubic ZrO_2 structure of the $P\bar{4}3m$ space group[39], the area enclosed by the yellow box can be regarded as a single-crystal grain of "pseudo" cubic ZrO_2 with the [011] zone axis along the incident beam or the normal of the specimen surface. The NBED pattern indicates the lattice constant of the nanoscale ZrO_2 layer is 0.50 nm. However, it has been reported that the lattice constants of standard orthorhombic ZrO_2 are 0.526, 0.507, and 0.508 nm along the *a*, *b*, and *c* axes, respectively[19]. Also, the standard cubic ZrO_2 has a lattice constant of 0.51 nm and a non-centrosymmetric structure due to ~0.03 nm displacements of the oxygen sublattices along <111> directions from $Fm\bar{3}m$[39]. Thus, it can be deduced that the nanoscale ZrO_2 layer is of non-centrosymmetric structure and compressively stressed comparing to either the orthorhombic phase or the "pseudo" cubic of the $P\bar{4}3m$ space group. These are consistent with the grazing incidence X-ray diffraction (GIXRD) pattern of the as-deposited *f*-ZrO_2 (12 nm) layer (Supplementary Figure 14 in Supplementary Information, Note 12), which shows a deviation of the X-ray diffraction (XRD) peak from the strain-free cubic or orthorhombic ZrO_2. Therefore, the results revealed by NBED and GIXRD patterns indicate the presence of the non-centrosymmetric structure and compressive strain in the nanoscale ZrO_2 layer, giving rise to the emergence of ferroelectricity[40–42]. Figure 4d shows the corresponding dark-field image taken by the reflection indicated by the red circle in Fig. 4c. A part of the ZrO_2 grain is bright by satisfying Bragg's condition of the $\bar{1}1\bar{1}$ reflection. Afterwards, the TEM sample was tilted to another angle to get more information. Figure 4e shows another bright-field image. The NBED pattern of the grain indicated by the yellow box in Fig. 4e is shown in Fig. 4f, which also agrees with the simulated diffraction pattern of standard cubic ZrO_2 with the $P\bar{4}3m$ space group along the $[\bar{1}12]$ zone axis. This NBED pattern indicates that the lattice constant is also 0.50nm. A dark-field image taken by the $1\bar{1}1$ reflection is displayed in Fig. 4g, where almost the grain indicated by the yellow box is bright. It should be noted that the regions with bright and dark contrast appear alternately in the ZrO_2 layer in Fig. 4d, g. The regions with bright contrast can be regarded as single-crystal grains with the same orientation, that is, the [011] zone axis in Fig. 4d and the $[\bar{1}12]$ in Fig. 4g. The regions with dark contrast are ZrO_2 grains whose orientation is different from the grains with bright contrast. In principle, the polarization directions are different between such single-crystal grains pretended to have the same crystal structure of $P\bar{4}3m$ in case their zone axes are different along a certain

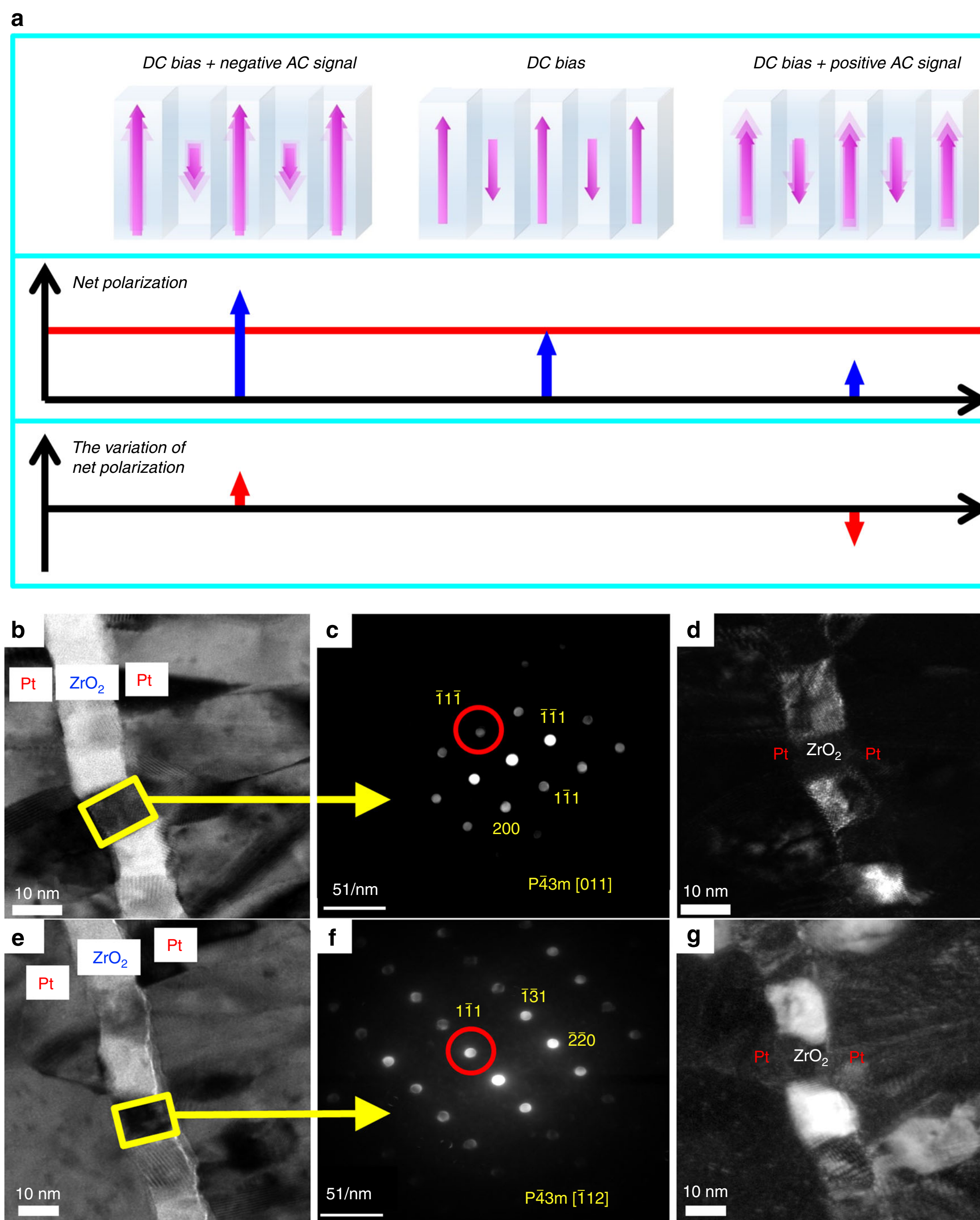

Fig. 4 Ferroelectric multi-domains. **a** Schematic diagrams of the ferroelectric multi-domains biased at a direct-current (DC) voltage and the switching of the net polarization variation under small-signal modulation. **b**–**g** Cross-sectional transmission electron microscope (TEM) images and nano-beam electron diffraction (NBED) patterns of the ferroelectric multi-domains in the as-deposited Pt/zirconium oxide (ZrO_2)/Pt MFM structure. **b** The bright-field TEM image. **c** The ZrO_2 NBED pattern of the enclosed area in **b** along the [011] zone axis. **d** The dark-field TEM image along the [011] zone axis. **e** The bright-field TEM image at another angle. **f** The ZrO_2 NBED pattern of the enclosed area in **e** along the [$\bar{1}12$] zone axis. **g** The dark-field TEM image along the [$\bar{1}12$] zone axis. The alternate bright and dark regions as seen in **d**, **g**) give a support of the ferroelectric multi-domains in the nanoscale ZrO_2 layer

direction (for instance, the normal of the layer). Accordingly, the appearance of bright and dark regions in a periodic manner gives a support of the presence of ferroelectric multi-domains in nano-*f*-ZrO_2.

In summary, the ferroelectric inductance and NC originating from polarization switching are manifested via both small- and large-signal operations of the as-deposited nano-*f*-ZrO_2 layer. On the one hand, nano-*f*-ZrO_2 yields a positive imaginary impedance and the capacitance enhancement as connected in series with a paraelectric capacitor, demonstrating the ferroelectric inductance and NC under small-signal modulation. The ferroelectric multi-domains, as observed in the NBED characterization, are responsible for the small-signal operation of the ferroelectric inductance and NC. On the other hand, the RLC responses of

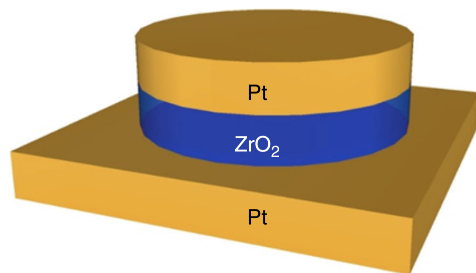

Fig. 5 Schematic diagram of the ZrO_2 MFM structure

nano-*f*-ZrO_2 and the sub-60 mV/dec SS of NC-JLTs are attributed to large-signal operations of the ferroelectric inductance and NC. The analysis based on Maxwell's equations shows that the charge redistribution caused by polarization switching contributes to an effective ferroelectric-induced emf, which reduces the voltage drop across the ferroelectric layer similar to the behavior described by Lenz's law. Therefore, the effective ferroelectric-induced emf is responsible for the inductive responses and NC of nano-*f*-ZrO_2. Contrary to conventional inductors based on spiral electric coils with large footprints and low inductance densities, the planar ferroelectric inductance provides a much larger inductance and occupies a much smaller area. Therefore, the ferroelectric inductance is beneficial to a broad range of applications such as wireless communications, radar, and RF-integrated circuits.

Methods

The MFM structure for the measurements of the *P–E* hysteresis loop, the time-domain voltage and current responses, and the Nyquist impedance plot. Figure 5 shows the schematic ZrO_2 MFM structure. The bottom Pt electrode was deposited by an electron beam evaporator on a Si substrate. Then a 12-nm *f*-ZrO_2 layer was deposited on the Pt electrode at 300 °C by the plasma ALD (Ultratech, Fiji). The tetrakis(dimethylamino)zirconium (TDMAZr, $Zr[N(CH_3)_2]_4$) and O_2 plasma were used as the precursor and reactant for zirconium and oxygen, respectively. Afterwards, the top Pt electrode was deposited on ZrO_2 by an RF sputtering.

Series connection of a paraelectric HfO_2 capacitor with a ZrO_2 capacitor for the enhancement of small-signal capacitance. Figure 3a shows the schematic diagram of the capacitor structures under test. All the top, internal, and bottom Pt electrodes were prepared by the RF sputtering. The paraelectric HfO_2 (~12 nm) and *f*-ZrO_2 (~12 nm) layers were deposited at 300 °C by the plasma ALD, while the *p*-ZrO_2 layer was deposited at a lower temperature of 250 °C in the same ALD chamber operated in thermal mode. The precursors for hafnium and zirconium were tetrakis(dimethylamino)hafnium (TDMAHf, $Hf[N(CH_3)_2]_4$) and TDMAZr, and the oxygen sources were O_2 plasma and H_2O vapor for the plasma and thermal ALD, respectively. The top and internal Pt electrodes with a radius of 70μm were defined by the photolithography and lift-off processes. The top and internal Pt electrodes were used as the hard masks for the subsequent removal of HfO_2 and ZrO_2 using the CHF_3 dry etching.

Fabrication of NC Si JLTs. Figure 1a shows the schematic structures of the NC Si JLT and the gate stack. The substrate is the silicon-on-insulator wafer with a 150-nm layer of buried oxide and a 70-nm top Si layer. First, the top Si layer was implanted with As^+ for the formation of a heavily doped n^+ Si channel with a doping concentration of $\sim 5 \times 10^{18}$ ions/cm^3. Subsequently, the Si channel was thinned down to ~20nm by multiple dry oxidation and wet buffered oxide etch. Next, the electron beam lithography and the CF_4 dry etching were carried out to define the width and the length of the Si channel. The Ω-shaped gate was then formed by the following dry oxidation and wet buffered oxide etch. The thickness and the shape of the resulting Si channel were confirmed by the cross-sectional TEM image as shown in Fig. 1b. The helium ion microscopy (Zeiss Orion NanoFab) was used to image the top-view morphology of the Si channel and contact pads. The final dimensions of the Si channel are about 70 nm in length, 50 nm in width, and 20 nm in thickness. Afterwards, the gate stack was deposited and defined by the lithography. The high-*K* HfO_2 (~6 nm), *f*-ZrO_2 (~12 nm), and metallic TiN layers were prepared by ALD at 300 °C. The precursors for hafnium, zirconium, and titanium were TDMAHf, TDMAZr, and tetrakis (dimethylamino) titanium ($Ti[N(CH_3)_2]_4$). The oxygen/nitrogen sources were H_2O vapor, O_2 plasma, and N_2/H_2 plasma for HfO_2, ZrO_2, and TiN, respectively. The Pt electrodes were prepared by the RF sputtering. Afterwards, the thermal evaporation, lift-off process, and rapid thermal annealing at 400 °C were utilized to form the NiSi contacts at the source and the drain.

Materials characterization. The cross-sectional TEM sample was prepared by the focused ion beam (FIB, Helios NanoLab 600i, FEI) system. Structural analysis of the ferroelectric layer was performed by the TEM (Tecnai G2 F20, FEI) with an acceleration voltage of 200kV. The bright/dark-field images and the NBED patterns were produced by the TEM with different focal planes. The NBED patterns were examined by the DigitalMicrograph (Gatan) software. The cross-sectional image of the gate stack was acquired by the SEM equipped in the FIB system. The crystalline phase of the ferroelectric ZrO_2 layer was identified using the GIXRD (TTRAX III, Rigaku).

Electrical characterization. The Keysight B1500A semiconductor parameter analyzer in the C_p-R_p mode was used to measure the electrical characteristics of the negative-capacitance Si JLTs and the small-signal capacitance of the *f*-ZrO_2/HfO_2, *p*-ZrO_2/HfO_2, and HfO_2 capacitors. The voltage and current responses in the time domain was probed by the Keysight B1500A equipped with the waveform generator/fast measurement unit module. The measurements were calibrated using the built-in "Module Self Calibration" in the Keysight B1500A analyzer. The ZrO_2 MFM structure was tested by the impedance analyzer (Autolab PGSTAT302N) to obtain the Nyquist plot. For the ferroelectric characterization, the *P–E* hysteresis curves were acquired using the ferroelectric analyzer (TF2000, aixACCT) operated at 2000 Hz.

Data availability

The data sets generated during and/or analyzed during the current study are available from the corresponding author on reasonable request.

Received: 5 May 2018 Accepted: 17 January 2019
Published online: 21 March 2019

References

1. Salahuddin, S. & Datta, S. Use of negative capacitance to provide voltage amplification for low power nanoscale devices. *Nano Lett.* **8**, 405–410 (2008).
2. Khan, A. I., Yeung, C. W., Hu, C. & Salahuddin, S. Ferroelectric negative capacitance MOSFET: capacitance tuning & antiferroelectric operation. In *Proc. IEEE Int. Electron Devices Meeting (IEDM)*, pp. 11.3.1–11.3.4 (2011).
3. Khan, A. I. et al. Negative capacitance in a ferroelectric capacitor. *Nat. Mater.* **14**, 182–186 (2015).
4. Appleby, D. J. et al. Experimental observation of negative capacitance in ferroelectrics at room temperature. *Nano Lett.* **14**, 3864–3868 (2014).
5. Dasgupta, S. et al. Sub-kT/q switching in strong inversion in $PbZr_{0.52}Ti_{0.48}O_3$ gated negative capacitance FETs. *IEEE J. Explor. Solid-State Comput. Dev. Circ.* **1**, 43–48 (2015).
6. Gao, W. et al. Room-temperature negative capacitance in a ferroelectric–dielectric superlattice heterostructure. *Nano Lett.* **14**, 5814–5819 (2014).
7. Li, K.-S., et al. Sub-60mV-swing negative-capacitance FinFET without hysteresis. In *Proc. IEEE Int. Electron Devices Meeting (IEDM)*, pp. 22.6.1–22.6.4 (2015).
8. McGuire, F. A. et al. Sustained sub-60 mV/decade switching via the negative capacitance effect in MoS_2 transistors. *Nano. Lett.* **17**, 4801–4806 (2017).
9. Si, M. et al. Steep-slope hysteresis-free negative capacitance MoS_2 transistors. *Nat. Nanotechnol.* **13.1**, 24 (2017).
10. Yeung, C. W., Khan, A. I., Cheng, J.-Y., Salahuddin, S. & Hu, C. Non-hysteretic negative capacitance FET with Sub-30mV/dec swing over 10^6X current range and I_{ON} of 0.3 mA/μm without strain enhancement at 0.3 V VDD. In *In Conf. Simul. Semicond. Processes Devices*, p. 257 (2012).
11. Rusu, A., Salvatore, G. A., Jiménez, D. & Ionescu, A. M. Metal–ferroelectric–meta-oxide–semiconductor field effect transistor with sub-60mV/decade subthreshold swing and internal voltage amplification. In *Electron Devices Meeting (IEDM), 2010 IEEE International* 16.3.1–16.3.4 (2010).
12. Islam Khan, A. et al. Experimental evidence of ferroelectric negative capacitance in nanoscale heterostructures. *Appl. Phys. Lett.* **99**, 113501 (2011).
13. Majumdar, K., Datta, S. & Rao, S. P. Revisiting the theory of ferroelectric negative capacitance. *IEEE Trans. Electron Dev.* **63**, 2043–2049 (2016).
14. Hoffmann, M. et al. Direct observation of negative capacitance in polycrystalline ferroelectric HfO_2. *Adv. Funct. Mater.* **26**, 8643–8649 (2016).
15. Yuan, Z. C. et al. Switching-speed limitations of ferroelectric negative-capacitance FETs. *IEEE Trans. Electron Dev.* **63**, 4046–4052 (2016).
16. Salvatore, G. A., Rusu, A. & Ionescu, A. M. Experimental confirmation of temperature dependent negative capacitance in ferroelectric field effect transistor. *Appl. Phys. Lett.* **100**, 163504 (2012).

17. Lee, M. et al. Prospects for ferroelectric $HfZrO_x$ FETs with experimentally CET= 0.98 nm, SS_{for}= 42mV/dec, SS_{rev}= 28mV/dec, switch-off<0.2 V, and hysteresis-free strategies. In *Proc. IEEE Int. Electron Devices Meeting (IEDM)*, pp. 5–22 (2015).
18. Muller, J. et al. Ferroelectricity in simple binary ZrO_2 and HfO_2. *Nano Lett.* **12**, 4318–4323 (2012).
19. Mueller, S. et al. Incipient ferroelectricity in Al-doped HfO_2 thin films. *Adv. Funct. Mater.* **22**, 2412–2417 (2012).
20. Hyuk Park, M. et al. Effect of forming gas annealing on the ferroelectric properties of $Hf_{0.5}Zr_{0.5}O_2$ thin films with and without Pt electrodes. *Appl. Phys. Lett.* **102**, 112914 (2013).
21. Hyuk Park, M. et al. Evolution of phases and ferroelectric properties of thin $Hf_{0.5}Zr_{0.5}O_2$ films according to the thickness and annealing temperature. *Appl. Phys. Lett.* **102**, 242905 (2013).
22. Schroeder, U. et al. Hafnium oxide based CMOS compatible ferroelectric materials. *ECS J. Solid State Sci. Technol.* **2**, N69–N72 (2013).
23. Hoffmann, M. et al. Low temperature compatible hafnium oxide based ferroelectrics. *Ferroelectrics* **480**, 16–23 (2015). **1**.
24. Lin, B.-T., Lu, Y.-W., Shieh, J. & Chen, M.-J. Induction of ferroelectricity in nanoscale ZrO_2 thin films on Pt electrode without post-annealing. *J. Eur. Ceram. Soc.* **37**, 1135–1139 (2017).
25. Alexander, C. K. & Sadiku, M. N. O. *Fundamentals of Electric Circuits* (McGraw-Hill Education, New York, 2016).
26. Bultel, Y., Géniès, L., Antoine, O., Ozil, P. & Durand, R. Modeling impedance diagrams of active layers in gas diffusion electrodes: diffusion, ohmic drop effects and multistep reactions. *J. Electroanal. Chem.* **527**, 143–155 (2002).
27. Makharia, R., Mathias, M. F. & Baker, D. R. Measurement of catalyst layer electrolyte resistance in PEFCs using electrochemical impedance spectroscopy. *J. Electrochem. Soc.* **152**, A970–A977 (2005).
28. Roy, S. K., Orazem, M. E. & Tribollet, B. Interpretation of low-frequency inductive loops in PEM fuel cells. *J. Electrochem. Soc.* **154**, B1378–B1388 (2007).
29. Antoine, O., Bultel, Y. & Durand, R. Oxygen reduction reaction kinetics and mechanism on platinum nanoparticles inside Nafion. *J. Electroanal. Chem.* **499**, 85–94 (2001).
30. Taibl, S., Fafilek, G. & Fleig, J. Impedance spectra of Fe-doped $SrTiO_3$ thin films upon bias voltage: inductive loops as a trace of ion motion. *Nanoscale* **8**, 13954–13966 (2016).
31. Guerrero, A. et al. Properties of contact and bulk impedances in hybrid lead halide perovskite solar cells including inductive loop elements. *J. Phys. Chem. C* **120**, 8023–8032 (2016).
32. Ghahremanirad, E., Bou, A., Olyaee, S. & Bisquert, J. Inductive loop in the impedance response of perovskite solar cells explained by surface polarization model. *J. Phys. Chem. Lett.* **8**, 1402–1406 (2017).
33. Lopez-Varo, P. et al. Device physics of hybrid perovskite solar cells: theory and experiment. *Adv. Energy Mater.* **8**, 1702772 (2018).
34. Gardner, D. S. et al. Review of on-chip inductor structures with magnetic films. *IEEE Trans. Magn.* **45**, 4760–4766 (2009).
35. Kasamatsu, S., Watanabe, S., Hwang, C. S. & Han, S. Emergence of negative capacitance in multidomain ferroelectric-paraelectric nanocapacitors at finite bias. *Adv. Mater.* **28**, 335–340 (2016).
36. Zubko, P. et al. Negative capacitance in multidomain ferroelectric superlattices. *Nature* **534**, 524–528 (2016).
37. Cheng, S.-Y. et al. Structure analysis of bismuth sodium titanate-based A-site relaxor ferroelectrics by electron diffraction. *J. Eur. Ceram. Soc.* **33**, 2141–2153 (2013).
38. Bursill, L. A., JuLin, P., Hua, Q. & Setter, N. Relationship between nanostructure and dielectric response of lead scandium tantalate—(I) structure and domain textures. *Phys. B* **205**, 305–326 (1995). (3-4).
39. McClellan, K. J., Xiao, S. Q., Lagerlof, K. P. D. & Heuer, A. H. Determination of the structure of the cubic phase in high-$ZrO_2Y_2O_3$-ZrO_2 alloys by convergent-beam electron diffraction. *Philos. Mag. A* **70**, 185–200 (1994).
40. Ball, B. L., Smith, R. C., Kim, S. J. & Seelecke, S. A stress-dependent hysteresis model for ferroelectric materials. *J. Intell. Mater. Syst. Struct.* **18**, 69–88 (2007).
41. Davis, M., Damjanovic, D. & Setter, N. Electric-field-, temperature-, and stress-induced phase transitions in relaxor ferroelectric single crystals. *Phys. Rev. B* **73**, 014115 (2006).
42. Pertsev, N., Tagantsev, A. & Setter, N. Phase transitions and strain-induced ferroelectricity in $SrTiO_3$ epitaxial thin films. *Phys. Rev. B* **61**, R825 (2000).

Acknowledgements

We acknowledge the financial support in part by Taiwan Semiconductor Manufacturing Company (TSMC) and the Ministry of Science and Technology, Taiwan (MOST 107-2218-E-002-045 and 106-2221-E-002-086-MY2).

Author contributions

M.-J.C. and S.C.P. conceived the idea and coordinated the project. M.-J.C. and P.-H.C. designed the experiments. Y.-T.Y. and P.-H.C. carried out the impedance and NBED measurements. P.-H.C. and I.-N.T. optimized the ALD process, fabricated the MFM structures, and performed the small-signal capacitance measurement. M.-J.C., P.-H.C. and C.-H.L. conducted the theoretical analysis. P.-H.C. fabricated and measured NC-JLTs. P.-H.C. conducted the cross-sectional TEM, SEM, and GIXRD measurements. J.S. provided the ferroelectric characterization. M.S. analyzed the NBED images. M.-J.C., P.-H.C., Y.-T.Y., M.S. and L.-JL. wrote the paper. All authors discussed the results and commented on the manuscript.

Additional information

Supplementary information accompanies this paper at https://doi.org/10.1038/s42005-019-0120-1.

Competing interests: The authors declare no competing interests.

Reprints and permission information is available online at http://npg.nature.com/reprintsandpermissions/

Publisher's note: Springer Nature remains neutral with regard to jurisdictional claims in published maps and institutional affiliations.

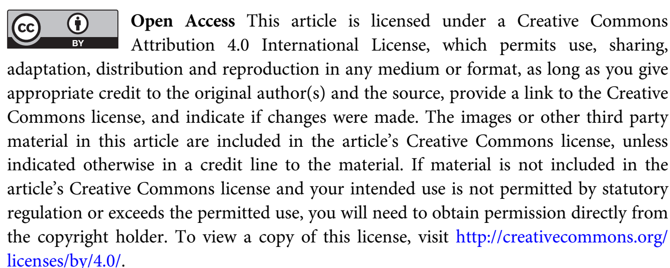

Open Access This article is licensed under a Creative Commons Attribution 4.0 International License, which permits use, sharing, adaptation, distribution and reproduction in any medium or format, as long as you give appropriate credit to the original author(s) and the source, provide a link to the Creative Commons license, and indicate if changes were made. The images or other third party material in this article are included in the article's Creative Commons license, unless indicated otherwise in a credit line to the material. If material is not included in the article's Creative Commons license and your intended use is not permitted by statutory regulation or exceeds the permitted use, you will need to obtain permission directly from the copyright holder. To view a copy of this license, visit http://creativecommons.org/licenses/by/4.0/.

© The Author(s) 2019